Air Force Institute of Technology

AFIT Scholar

Faculty Publications

10-2015

Semianalytical Solutions for Transport in Aquifer and Fractured Clay Matrix System

Junqi Huang

Mark N. Goltz
Air Force Institute of Technology

Follow this and additional works at: https://scholar.afit.edu/facpub

Part of the Water Resource Management Commons

Recommended Citation

Huang, J., & Goltz, M. N. (2015). Semianalytical solutions for transport in aquifer and fractured clay matrix system. Water Resources Research, 51(9), 7218–7237. https://doi.org/10.1002/2014WR016073

This Article is brought to you for free and open access by AFIT Scholar. It has been accepted for inclusion in Faculty Publications by an authorized administrator of AFIT Scholar. For more information, please contact AFIT.ENWL.Repository@us.af.mil.

AGU PUBLICATIONS

Water Resources Research

RESEARCH ARTICLE

10.1002/2014WR016073

Key Points:
- Semianalytical model for transport in a dual-layer aquifer system
- Diffusive exchange between the fractures and the low-permeability matrix
- Insights into process of back diffusion from the fractured clay formation

Supporting Information:
- Supporting Information S1
- Software S1

Correspondence to:
J. Huang,
huang.junqi@epa.gov

Citation:
Huang, J., and M. N. Goltz (2015), Semianalytical solutions for transport in aquifer and fractured clay matrix system, *Water Resour. Res.*, *51*, 7218–7237, doi:10.1002/2014WR016073.

Received 30 JUN 2014
Accepted 4 AUG 2015
Accepted article online 7 AUG 2015
Published online 6 SEP 2015

© 2015. American Geophysical Union. All Rights Reserved.

Semianalytical solutions for transport in aquifer and fractured clay matrix system

Junqi Huang[1] and Mark N. Goltz[2]

[1]Ground Water and Ecosystems Restoration Division, National Risk Management Research Laboratory, U.S. Environmental Protection Agency, Ada, Oklahoma, USA, [2]Department of Systems Engineering and Management, Air Force Institute of Technology, Dayton, Ohio, USA

Abstract A three-dimensional mathematical model that describes transport of contaminant in a horizontal aquifer with simultaneous diffusion into a fractured clay formation is proposed. A group of semianalytical solutions is derived based on specific initial and boundary conditions as well as various source functions. The analytical model solutions are evaluated by numerical Laplace inverse transformation and analytical Fourier inverse transformation. The model solutions can be used to study the fate and transport in a three-dimensional spatial domain in which a nonaqueous phase liquid exists as a pool atop a fractured low-permeability clay layer. The nonaqueous phase liquid gradually dissolves into the groundwater flowing past the pool, while simultaneously diffusing into the fractured clay formation below the aquifer. Mass transfer of the contaminant into the clay formation is demonstrated to be significantly enhanced by the existence of the fractures, even though the volume of fractures is relatively small compared to the volume of the clay matrix. The model solution is a useful tool in assessing contaminant attenuation processes in a confined aquifer underlain by a fractured clay formation.

1. Introduction

Efforts to remediate groundwater contaminated with dense nonaqueous phase liquids (DNAPLs) continue to fail [*AFCEE*, 2007]. These failures have, at least in some cases, been attributed to diffusion of dissolved DNAPL into low-permeability layers, with subsequent back diffusion of the dissolved DNAPL after DNAPL in the accessible high-permeability zones has been remediated [*Wilson*, 1997; *Ball et al.*, 1997; *Liu and Ball*, 2002; *Sale et al.*, 2008; *Parker et al.*, 2008]. The conventional approach to modeling back diffusion is to assume diffusion into and out of a competent low-permeability zone [*Feenstra et al.*, 1996; *Chapman and Parker*, 2005; *Seyedabbasi et al.*, 2012]. In reality, however, it is quite possible that the low-permeability zone will not be competent. Cracks, which occur naturally in clay layers, can be caused by releases of pressure due to erosion, excavation, or changes in water table levels [*McKay et al.*, 1993]. It has also been demonstrated that the presence of pooled DNAPL atop low-permeability clay may result in fracturing of the clay [*Ayral et al.*, 2014]. Clearly, modeling diffusion and back diffusion into competent low-permeability zones is a simplification that may not be appropriate at many sites. The goal of this study is to develop and apply a model that can be used to simulate the effect of fractures in a low-permeability zone on back diffusion, and subsequently, on the evolution of a dissolved contaminant plume. To achieve this goal, we present an analytical solution of a model that simulates advection-dispersion-adsorption transport of a dissolved contaminant in a high-permeability layer originating from a DNAPL source zone, coupled to a model that simulates diffusion in the fractures of a low-permeability layer along with diffusive exchange of contaminant between the fractures and the low-permeability matrix (see Figure 1). While an analytical solution requires a number of simplifications that may make it unsuitable for specific field applications [*Javandel et al.*, 1984], such solutions have been found to be quite useful in: (1) analysis of solute transport behavior by means of the model [*Goltz and Roberts*, 1987], (2) verifying more complex numerical models [e.g., *Oreskes et al.*, 1994], and (3) efficiently and simply obtaining order of magnitude estimates [*Javandel et al.*, 1984].

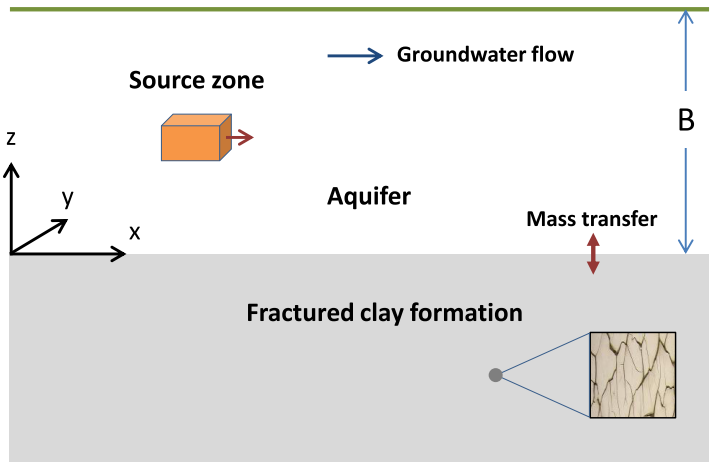

Figure 1. Conceptual model of NAPL transport in an aquifer underlain by a fractured clay formation.

2. Model Equations

2.1. Transport in Aquifer

The transport of a reacting and absorbing dissolved compound in a horizontal aquifer can be described by the following equations [*Goltz and Roberts*, 1986]:

$$\theta\frac{\partial C}{\partial t}+\rho_b\frac{\partial S}{\partial t}=D_x\frac{\partial^2 C}{\partial x^2}-v\frac{\partial C}{\partial x}+D_y\frac{\partial^2 C}{\partial y^2}+D_z\frac{\partial^2 C}{\partial z^2}-\lambda_w\theta C-\lambda_s\rho_b S+q \tag{1a}$$

$$\frac{\partial S}{\partial t}=\alpha(k_d C-S)-\lambda_s S \tag{1b}$$

where, C is the dissolved contaminant concentration (mg/L); S is the absorbed contaminant concentration (mg/kg); θ is the porosity of the aquifer; ρ_b is the bulk density of the aquifer solids (kg/L); D_x, D_y, and D_z are the dispersion coefficients in the x, y, and z directions, respectively (m^2/day); v is the groundwater velocity in the x direction (m/day); λ_w is a first-order decay constant of dissolved contaminant (1/day); λ_s is a first-order decay constant of absorbed contaminant (1/day); α is a first-order rate coefficient describing mass transfer between dissolved and solid phases (1/day); k_d is a distribution coefficient describing equilibrium partitioning between absorbed and dissolved phases (L/kg); q is a source term (mg/(L-day)); t is time (day); x, y, z are spatial coordinates (m).

2.2. Transport in Fractured Clay Formation

We simulate transport in the fractured clay formation assuming vertical diffusion in the fractures coupled with slower diffusion within the clay matrix.

Equations (2a) and (2b) model diffusion/sorption/degradation in the fracture and matrix system, respectively, with the last term on the right-hand side of both equations describing the rate of mass exchange between the fracture and the matrix [*Bear*, 1979; *Chen*, 1986]. Equation (2c) describes rate-limited sorption and sorbed phase degradation of contaminant in the matrix.

$$\theta_f\frac{\partial C_f}{\partial t}=D_f\frac{\partial^2 C_f}{\partial z^2}-\theta_f\lambda_f C_f-\kappa(C_f-C_m) \tag{2a}$$

$$\theta_m\frac{\partial C_m}{\partial t}+\rho_m\frac{\partial S_m}{\partial t}=D_m\frac{\partial^2 C_m}{\partial z^2}-\theta_m\lambda_m C_m-\rho_m\lambda_{sm}S_m+\kappa(C_f-C_m) \tag{2b}$$

$$\frac{\partial S_m}{\partial t}=\alpha_m(k_m C_m-S_m)-\lambda_{sm}S_m \tag{2c}$$

where, C_f is the dissolved contaminant concentration in the fracture (mg/L); C_m is the dissolved contaminant concentration in the matrix (mg/L); S_m is the absorbed contaminant concentration in the matrix (mg/kg); θ_f and θ_m are respectively the porosity of the fracture and matrix; D_f and D_m are respectively the effective diffusion coefficients in the fracture and matrix (m^2/day); ρ_m is the bulk density of the matrix solids (kg/L); λ_f is a first-order decay constant of dissolved contaminant in fractures (1/day); λ_m is a first-order decay constant of dissolved contaminant in the matrix (1/day); λ_{sm} is a first-order decay constant of absorbed contaminant in the matrix (1/day); α_m is the rate-limited adsorption coefficient in the matrix (1/day); k_m is a distribution coefficient describing equilibrium partitioning between absorbed and dissolved phases in the matrix (L/kg); and κ is a first-order mass transfer rate coefficient describing the mass exchange between the fracture and the matrix (1/day).

2.3. Initial Conditions

Initially, due to the presence of the DNAPL, we assume there is a distribution of dissolved DNAPL in the aquifer described by a function $f(x, y, z)$:

$$C=f(x,y,z),\ t=0,\ -\infty \le x,y < \infty,\ 0 \le z \le B \tag{3a}$$

where B is the thickness of the aquifer.

Initial equilibrium condition requires $S=k_dC$, which leads to:

$$S=k_df(x,y,z),\ t=0,\ -\infty \le x,y < \infty,\ 0 \le z \le B \tag{3b}$$

In the fractured clay layer, we assume there is no initial contaminant distribution:

$$C_f=0,\ t=0,\ -\infty \le x,y < \infty,\ -\infty \le z < 0 \tag{3c}$$

$$C_m=0,\ t=0,\ -\infty \le x,y < \infty,\ -\infty \le z < 0 \tag{3d}$$

$$S_m=0,\ t=0,\ -\infty \le x,y < \infty,\ -\infty \le z < 0 \tag{3e}$$

2.4. Boundary Conditions

Equation (4a) specifies no vertical flux at the top of the aquifer:

$$\frac{\partial C}{\partial z}=0,\ z=B,\ -\infty < x,y < \infty,\ t > 0 \tag{4a}$$

Equations (4b), (4c), and (4d) specify that far from the source, contaminant concentration is assumed to be zero:

$$C=0,\ x,y \to \pm\infty,\ 0 \le z \le B,\ t > 0 \tag{4b}$$

$$C_f=0,\ z \to -\infty,\ -\infty < x,y < \infty,\ t > 0 \tag{4c}$$

$$C_m=0,\ z \to -\infty,\ -\infty < x,y < \infty,\ t > 0 \tag{4d}$$

Equations (4e) and (4f) couple equations (1) and (2), specifying that concentration and flux, respectively, at the interface between the aquifer and the underlying low-permeability layer, are equal:

$$C=C_f=C_m,\ z=0,\ -\infty < x,y < \infty,\ t > 0 \tag{4e}$$

$$D_z\frac{\partial C}{\partial z}=D_f\frac{\partial C_f}{\partial z}+D_m\frac{\partial C_m}{\partial z},\ z=0,\ -\infty < x,y < \infty,\ t > 0 \tag{4f}$$

2.5. Source Functions

Only linear source functions are amenable to analytical solution. Two common source functions are considered in the model.

2.5.1. Slug Mass Loading

The mass loading rate in a source area Ω_s is mathematically defined by a source function:

$$q=q_0[1-u(t-t_p)]\,g(x,y,z) \tag{5}$$

where q_0 is a constant rate of contaminant introduced into the aquifer [(mg/(L-d)], $g(x,y,z)$ is a switch function defined as:

$$g(x,y,z)=\begin{cases} 1, & x,y,z \in \Omega_s \\ 0 & x,y,z \notin \Omega_s \end{cases}$$

$u(\cdot)$ is the Heaviside function for a pulse input of duration t_p (day).

2.5.2. Dissolution Mass Loading

Most models describe the dissolution of DNAPL with a first-order rate law [*Imhoff and Miller*, 1996; *Imhoff et al*. 2003; *Clement et al*., 2004]

$$\rho_N\frac{\partial s_N}{\partial t}=-k_Ns_N^{\sigma}(C_s-C) \tag{6}$$

where, ρ_N is the density of DNAPL (mg/L), s_N is the saturation of DNAPL, k_N is the mass transfer rate coefficient (1/day) in the porous media, σ is a constant ($\ge$0), C_s is the solubility of DNAPL, C is the concentration in bulk water. Considering $C \ll C_s$, neglecting C may simplify (6):

$$\rho_N \frac{\partial s_N}{\partial t} = -k_N C_s s_N^{\sigma} \tag{7}$$

The similar expression for describing the time-dependent discharge of contaminant from a DNAPL source zone can be found in the works of *Parker and Park* [2004], *Zhu and Sykes* [2004], and *Falta et al.* [2005]. Integrating (7) subject to an initial condition gives

$$\rho_N \frac{\partial s_N}{\partial t} = \begin{cases} -k_N C_s s_{N0} \exp(-\eta t), & \sigma = 1 \\ -k_N C_s [(\sigma-1)\eta t + s_{N0}^{1-\sigma}]^{\sigma/(1-\sigma)}, & \sigma \neq 1 \end{cases} \tag{8}$$

where, $\eta = k_N C_s / \rho_N$, s_{N0} is the initial saturation of DNAPL.

The source function in the aquifer will be:

$$q(x,y,z,t) = -\theta \rho_N \frac{\partial s_N}{\partial t} g(x,y,z) = \begin{cases} \theta k_N C_s s_{N0} \exp(-\eta t) g(x,y,z), & \sigma = 1 \\ \theta k_N C_s [(\sigma-1)\eta t + s_{N0}^{1-\sigma}]^{\sigma/(1-\sigma)} g(x,y,z), & \sigma \neq 1 \end{cases} \tag{9}$$

For the case $\sigma < 1$, the dissolution process is finite, i.e., when $t = s_{N0}^{1-\sigma}/(1-\sigma)\eta$, the mass would be totally released and the source area cleaned up. For the case $\sigma \geq 1$, dissolution continues forever.

3. Model Solutions

3.1. Laplace Domain Solutions for Concentration

Applying the Laplace transform with respect to t, the Fourier transform with respect to x and y, and Fourier Sine transform with respect to z, equations (1) and (2) subject to the initial conditions (3) and boundary conditions (4) may be solved to obtain the solutions (see Appendix A):

$$\bar{C}(x,y,z,p) = \frac{1}{4\pi^2} \int_{-\infty}^{\infty} \int_{-\infty}^{\infty} \tilde{\bar{C}}(\hat{x},\hat{y},z,p) \exp[i(\hat{x}x + \hat{y}y)] d\hat{x} d\hat{y} \tag{10a}$$

$$\bar{C}_f = [F_1 \exp(\sqrt{r_1} z) + F_2 \exp(\sqrt{r_2} z)] \bar{C}(x,y,0,p) \tag{10b}$$

$$\bar{C}_m = [M_1 \exp(\sqrt{r_1} z) + M_2 \exp(\sqrt{r_2} z)] \bar{C}(x,y,0,p) \tag{10c}$$

$$\tilde{\bar{C}}(\hat{x},\hat{y},z,p) = d_1 \exp(-rz) + d_2 \exp(rz) + u(z) \tag{11a}$$

$$u(z) = -1/(2D_z r) \left\{ \int_0^z \exp[r(z'-z)] H(\hat{x},\hat{y},z',p) dz' + \int_z^B \exp[r(z-z')] H(\hat{x},\hat{y},z',p) dz' \right\} \tag{11b}$$

$$H(\hat{x},\hat{y},z,p) = -\psi(p) \tilde{f}(\hat{x},\hat{y},z) - \phi(p) \tilde{g}(\hat{x},\hat{y},z) \tag{11c}$$

where the variables with the bar indicate the Laplace transform, and the variables with the tilde indicate the Fourier transform; p is the Laplace transform parameter; $\hat{x}$ and $\hat{y}$ are the Fourier transform parameters; F_1, F_2, M_1, M_2, r_1 and r_2, d_1, d_2, r, ψ, and ϕ are dependent variables of p defined in Appendix A.

3.2. Laplace Domain Solutions for Mass

The rate of mass transfer through a horizontal plane ($z = const$) may be calculated as:

$$\bar{r}_{mass} = \int_{-\infty}^{\infty} \int_{-\infty}^{\infty} [-D_z \partial \bar{C}(x,y,z,p)/\partial z] dx dy, \; 0 \leq z \leq B \tag{12a}$$

$$\bar{r}_{mass} = \int_{-\infty}^{\infty} \int_{-\infty}^{\infty} [-D_f \partial \bar{C}_f(x,y,z,p)/\partial z - D_m \partial \bar{C}_m(x,y,z,p)/\partial z] dx dy, \; -\infty < z \leq 0 \tag{12b}$$

Based on the theory of Fourier transform [*Arfken*, 1985], the central ordinate value is represented as:

$$\tilde{\bar{C}}(0,0,z,p) = \int_{-\infty}^{\infty} \int_{-\infty}^{\infty} \bar{C}(x,y,z,p) dx dy \tag{13}$$

Using (13), (12) becomes:

$$\bar{r}_{mass} = -D_z \frac{\partial}{\partial z} \tilde{\bar{C}}(0,0,z,p),\ 0 \le z \le B \tag{14a}$$

$$\bar{r}_{mass} = -\Omega \tilde{\bar{C}}(0,0,z,p),\ -\infty \le z \le 0 \tag{14b}$$

where,

$$\Omega = [(D_f F_1 + D_m M_1)\sqrt{r_1}\exp(\sqrt{r_1}z) + (D_f F_2 + D_m M_2)\sqrt{r_2}\exp(\sqrt{r_2}z)]$$

For a given time t, the accumulated mass that has passed through the plane is:

$$\bar{A}^p_{mass} = \bar{r}_{mass}/p \tag{15}$$

For the plane at the bottom of the aquifer ($z = 0$), (14) has the form:

$$\begin{gathered} \bar{r}_{mass} = \beta_0 \int_0^B \int_{-\infty}^{\infty} \int_{-\infty}^{\infty} \cosh[r_0(B-z)][\psi f(x,y,z) + \phi g(x,y,z)]\, dxdydz \\ \beta_0 = (R+1)/[\exp(-r_0 B)R + \exp(r_0 B)] \\ r_0 = [\mu(p)/D_z]^{1/2} \end{gathered} \tag{16}$$

Equations (16) and (15) can be used, respectively, to evaluate the rate of mass transfer into the fractured clay from the aquifer, and the total mass that has entered the fractured clay at time t.

When $t \to \infty$, according to the final value theorem of Laplace transform, the total mass that passed through the bottom plane of the aquifer would be calculated as

$$A^{\infty}_{mass} = \lim_{p \to 0} (p\bar{A}^p_{mass}) = \bar{r}_{mass}|_{p=0} \tag{17}$$

For the case of no decay, i.e., λ_w, λ_s, λ_f, and λ_m are zero, consequently $r_0 = 0$, (17) would be

$$A^{\infty}_{mass} = \psi_0 \int_0^B \int_{-\infty}^{\infty} \int_{-\infty}^{\infty} f dxdydz + \phi_0 \int_0^B \int_{-\infty}^{\infty} \int_{-\infty}^{\infty} g dxdydz = \psi_0 C_T + \phi_0 V_T \tag{18}$$

where,

$$\psi_0 = 1 + \rho_b k_d/\theta$$

$$\phi_0 = \begin{cases} q_0 t_p, & \text{slug mass loading source} \\ \theta \rho_N s_{N0}, & \text{linear dissolution source} \end{cases}$$

C_T is the dissolved mass initially in the aquifer at $t = 0$ and V_T is the total volume of the source zone in the aquifer.

If we include degradation, subtracting (17) from (18) would give the total mass that has degraded

$$A^{\infty}_{\text{deg}} = \psi_0 C_T + \phi_0 V_T - \bar{r}_{mass}|_{p=0} \tag{19}$$

4. Evaluation of Model Solutions

Numerical Laplace inverse transform of (10) can be used to evaluate the solutions in time. One algorithm that is described by *de Hoog et al.* [1982] and has been implemented in MATLAB by *Hollenbeck* [1998] is employed in this study.

4.1. Inverse Fourier Transform

Theoretically, direct evaluation of the integrals in (A43) may be used to obtain the solutions in the Laplace domain. However, because of the oscillation of integrands, the numerical integration generally becomes inefficient. Analytical integration may be implemented in a grid system of space $(\hat{x}, \hat{y})$ on which $\tilde{\bar{C}}$ is expected to be represented by a simple interpolant in a grid cell. It is noticed that the major factor of oscillation is attributed to $\tilde{f}$ and $\tilde{g}$, which suggests that the separation of these oscillation factors from the solutions may improve the algorithm. Specifically, (A43) may be rewritten as:

$$\tilde{\bar{C}} = \int_0^B G(\hat{x}, \hat{y}, z, z', p) H(\hat{x}, \hat{y}, z', p) dz' \tag{20}$$

where,

$$G(\hat{x}, \hat{y}, z, z', p) = (2D_z r)^{-1} \{U(z)\exp(-rz') + V(z)\exp[-r(B-z')] - F(z, z')\}$$

$$U(z) = R\{\exp[-r(B-z)] + \exp[r(B-z)]\} / [\exp(-rB)R + \exp(rB)]$$

$$V(z) = [\exp(-rz)R - \exp(rz)] / [\exp(-rB)R + \exp(rB)]$$

$$F(z, z') = \begin{cases} \exp[-r(z-z')], & 0 \le z' \le z \\ \exp[-r(z'-z)], & z \le z' \le B \end{cases}$$

Generally, the function G has much less oscillations in the frequency domain $(\hat{x}, \hat{y})$ than $\tilde{\bar{C}}$, and may be inversely transformed without high-resolution sampling. Defining $\Gamma(x, y, z, z', p)$ as the inverse Fourier transform of $G(\hat{x}, \hat{y}, z, z', p)$ and $h(x, y, z', p)$ as the inverse Fourier transform of $H(\hat{x}, \hat{y}, z', p)$, according to the convolution principle of Fourier transform, the inverse Fourier transform of (20) is:

$$\bar{C} = \int_0^B \Gamma(x, y, z, z', p) * h(x, y, z', p) dz' \tag{21}$$

where the operator $*$ indicates a 2-D convolution.

Because G has the characteristic of an exponential function, it is significantly distributed in a limited region: $\hat{x}_{\min} < \hat{x} < \hat{x}_{\max}$ and $\hat{y}_{\min} < \hat{y} < \hat{y}_{\max}$ beyond which the function vanishes. Based upon these characteristics, the inverse Fourier transform of G becomes:

$$\Gamma(x, y, z, z', p) = \frac{1}{2\pi^2} \sum_{n=1}^{N} \int_{\hat{y}_{n1}}^{\hat{y}_{n2}} \int_{\hat{x}_{n1}}^{\hat{x}_{n2}} G(\hat{x}, \hat{y}, z, z', p) \exp(i\hat{x}x) \cos(\hat{y}y) d\hat{x} d\hat{y} \tag{22}$$

where, n is the subdomain number, N is the total number of subdomains in the region $\hat{x}_{\min} < \hat{x} < \hat{x}_{\max}$ and $0 < \hat{y} < \hat{y}_{\max}$, $\hat{x}_{nk}$ and $\hat{y}_{nk}$ (k = 1,2) are the coordinates of indices of the grid cell n. In (22), the fact that G is an even function of $\hat{y}$ is considered, so by symmetry it is only necessary to evaluate over the half interval $(0, \hat{y}_{\max})$. In a regular subdomain n (e.g., a rectangular grid cell), the function G can be expressed with a bilinear interpolant [*Chang*, 2009]:

$$\begin{aligned} G(\hat{x}, \hat{y}, z, z', p) = [&G(\hat{x}_{n1}, \hat{y}_{n1}, z, z', p)(\hat{x}_{n2} - \hat{x})(\hat{y}_{n2} - \hat{y}) + \\ &G(\hat{x}_{n2}, \hat{y}_{n1}, z, z', p)(\hat{x} - \hat{x}_{n1})(\hat{y}_{n2} - \hat{y}) + \\ &G(\hat{x}_{n1}, \hat{y}_{n2}, z, z', p)(\hat{x}_{n2} - \hat{x})(\hat{y} - \hat{y}_{n1}) + \\ &G(\hat{x}_{n2}, \hat{y}_{n2}, z, z', p)(\hat{x} - \hat{x}_{n1})(\hat{y} - \hat{y}_{n1})] / [(\hat{x}_{n2} - \hat{x}_{n1})(\hat{y}_{n2} - \hat{y}_{n1})] \end{aligned} \tag{23}$$

Using (23), the integration operation in (22) can be analytically performed in a grid cell. According to the definition of convolution,

$$\Gamma(x, y, z, z', p) * h(x, y, z', p) = \frac{1}{2\pi^2} \sum_{n=1}^{N} \int_{\hat{y}_{n1}}^{\hat{y}_{n2}} \int_{\hat{x}_{n1}}^{\hat{x}_{n2}} G(\hat{x}, \hat{y}, z, z', p) T(\hat{x}, \hat{y}, z', x, y) d\hat{x} d\hat{y} \tag{24}$$

$$T(\hat{x}, \hat{y}, z', x, y) = \int_{-\infty}^{+\infty} \int_{-\infty}^{+\infty} \exp[i\hat{x}(x - x')] \cos[\hat{y}(y - y')] h(x', y', z', p) dx' dy' \tag{25}$$

Function h contains the initial concentration $f(x, y, z)$ and source function $g(x, y, z)$. If h is approximated with a bilinear interpolant represented by (23), then (25) can be analytically integrated (see Appendix B). Consequently, by substituting (25) into (24), the integrations included in (24) also can be performed analytically.

4.2. Model Solution Verification

The three-dimensional analytical solutions developed here were verified by using two numerical code benchmarks, AT123D [*Yeh*, 1981] and MT3DMS [*Zheng and Wang*, 1999]. Because of limitations in the

Table 1. Model Parameter Values Used for Simulations

Parameter	θ	ρ_b (kg/L)	α (1/day)	k_d (L/kg)	λ_w (1/day)	λ_s (1/day)	v (m/d)
Value	0.3	1.76	0.05	1.8	3E-4	4E-4	0.5
Parameter	D_x (m^2/day)	D_y (m^2/day)	D_z (m^2/day)	θ_f	D_f (m^2/day)	λ_f (1/day)	θ_m
Value	1.0	0.2	0.1	0.05	7.8E-5	2E-4	0.4
Parameter	D_m (m^2/day)	λ_m (1/day)	α_m (1/day)	k_m (m)	ρ_m (kg/L)	λ_{sm} (1/day)	κ (1/day)
Value	2.6E-5	2E-4	0.03	2.3	2.0	1E-4	0.006

Table 2. Parameters Used to Define Initial Condition

Parameter	C_0 (mg/L)	B (m)	x_a (m)	x_b (m)	y_a (m)	y_b (m)	z_a (m)	z_b (m)
Value	100	5	−4	0	−2	2	1	3

Table 3. Parameters for Source Function

Parameter	q_0 (mg/(L-day))	t_p (day)	k_N (1/day)	C_s (mg/L)	σ	s_{N0}	ρ_N (kg/L)
Value	50	300	9	1100	1.0	0.034	1.46

numerical codes, the model scenarios were simplified, as specified below. In addition, the complete analytical solution (without simplification) is further verified by application of a newly developed numerical model.

The solution with simplified conditions is compared with an existing solution provided in AT123D [*Yeh*, 1981]. The modified AT123D code, AT123D-AT [*Burnell et al.* 2012] was used to evaluate the model subject to the appropriate initial and boundary conditions, as well as source function. Using parameter values given in Tables 1 and 2 while setting D_f, α, λ_w, λ_s to zero, and using the values for q_0 and t_p given in Table 3 (assuming the source function takes the form of slug mass loading as described by equation (5)), the model solution would be simplified to represent transport in a three-dimensional aquifer with finite thickness and uniform groundwater velocity. This solution would be available in AT123D-AT. The comparison for concentration breakthrough at two down gradient receptors is depicted in Figure 2a. The excellent match with the accepted solution gives confidence in the correctness of the analytical solution subject to the specified simplifications.

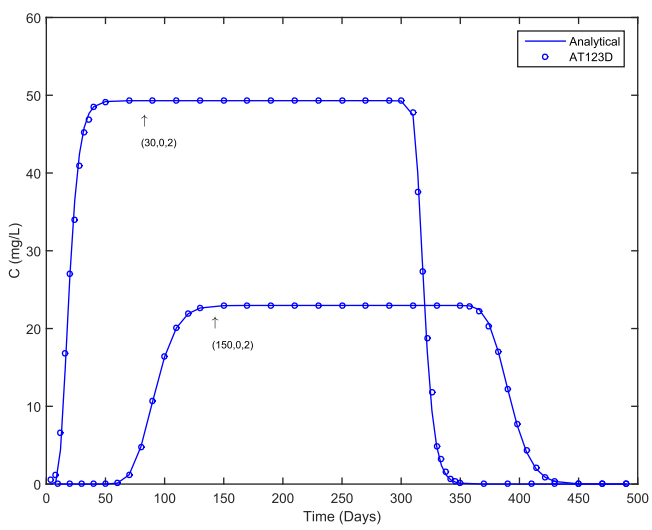

Figure 2a. Concentration breakthrough curves comparing the three-dimensional analytical solution and an existing solution (AT123D-AT) at down gradient observation points in the high-permeability zone for a slug mass loading source function and simplifications described in the text, The numbers in parentheses (*x, y, z*) represent the coordinates (in meters) of the down gradient observation points.

The solution is further compared with a numerical model, MT3DMS [*Zheng and Wang*, 1999]. To permit comparison of the two models, a simplification for the analytical solution is required; specifically, setting D_f and κ to zero to disable transport through the fractures, i.e., transport in the clay formation occurs only in the matrix system. Also, in consideration of the fact that diffusion only occurs in the vertical direction in the clay formation, MT3DMS is modified to disable molecular diffusion in the horizontal direction in the clay. The modified MT3DMS would appropriately simulate transport in a three-dimensional aquifer underlain by a competent clay formation. The specific settings for the numerical model include: (1) establishing horizontal (*x* direction) groundwater flow in the aquifer, no flow in

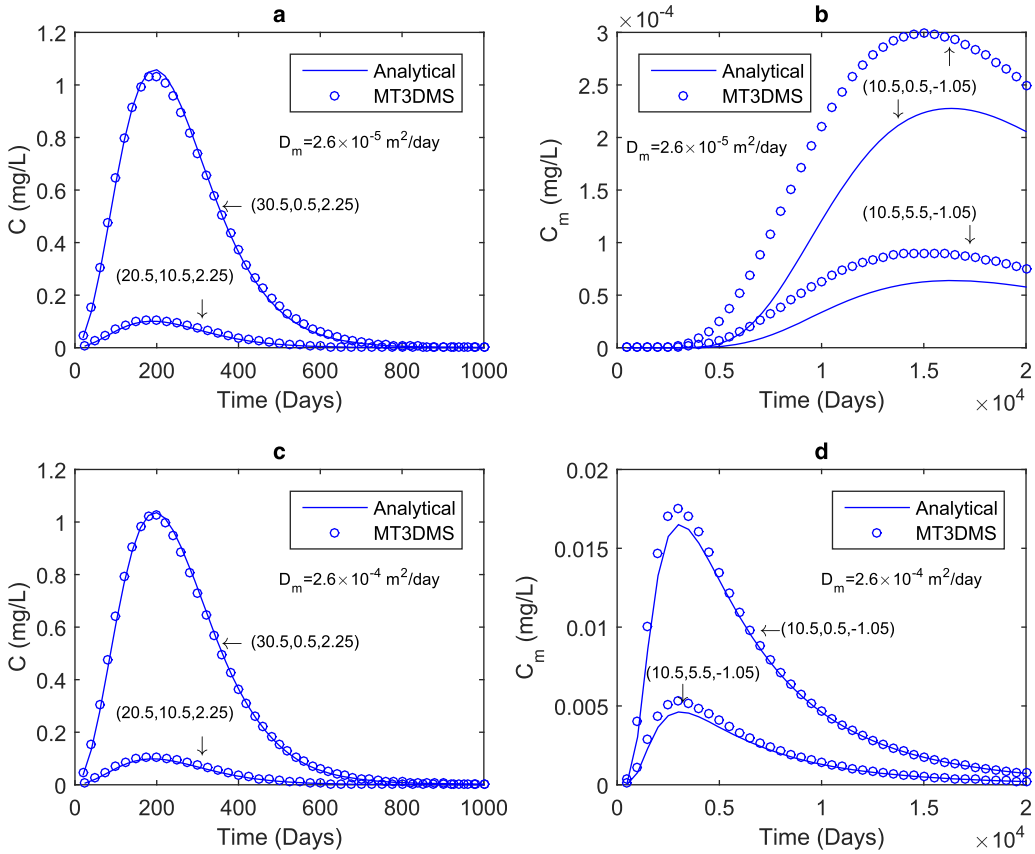

Figure 2b. Concentration breakthrough curves comparing the three-dimensional analytical solution without fractures and MT3DMS at two down gradient observation points in the high-permeability zone for (a) low and (c) high values of the diffusion coefficient (D_m), and comparing the three-dimensional analytical solution without fractures and MT3DMS at two down gradient observation points in the low-permeability zone for (b) low and (d) high values of the diffusion coefficient (D_m). The initial concentration distributes in a regular domain (simple initial condition). The numbers in parentheses (*x, y, z*) represent the coordinates (in meters) of the down gradient observation points.

the clay formation, (2) specifying the nonequilibrium sorption model parameters ρ_b, β, and k_d defined in MT3DMS, where the equivalence between these parameters and the analytical model parameters are: $\rho_b \sim \rho_b$ in the aquifer and $\rho_b \sim \rho_m$ in the clay formation; $\beta \sim \rho_b k_d \alpha$ in the aquifer and $\beta \sim \rho_m k_d \alpha_m$ in the clay formation; $k_d \sim k_d$ in the aquifer and $k_d \sim k_m$ in the clay formation, (3) setting the model geometric domain as $-20\ \text{m} \le x \le 100\ \text{m}$, $0\ \text{m} \le y \le 30\ \text{m}$, $-10\ \text{m} \le z \le 3\ \text{m}$, with a grid size of $\Delta x = 0.5$ m, $\Delta y = 0.5$ m, $\Delta z = 0.5$ m in the aquifer and $\Delta z = 0.1$ m in the clay formation, with 240 rows (*x* direction), 60 columns (*y* direction) and 40 layers (10 in the aquifer and 30 in the clay formation). Using parameter values given in Tables 1 and 2 subject to the initial conditions described by equation (3), the modified MT3DMS was run to simulate 20,000 days of transport. The comparison for concentration breakthrough with two different diffusion coefficients (D_m) at four down gradient observation points is depicted in Figure 2b. It is observed that the match between the analytical solution and the numerical solution is excellent for two locations in the high-permeability zone for both small and large D_m (Figures 2b(a) and 2b(c)), is reasonable for two locations in the low-permeability zone for large D_m (Figure 2b(d)), and has some error in the two low-permeability zone locations for small D_m (Figure 2b(b)). As indicated in the supporting information (see supporting information), the error shown in Figure 2b(b) is caused by the linear interpolation for the diffusion coefficient between grid cells in MT3DMS which generally overestimates the parameter value in the highly heterogeneous media (the parameter value change from $D_z = 0.1$ m^2/d in the aquifer to $D_m = 2.6 \times 10^{-5}$ m^2/d in the clay formation). The goodness of the comparisons depicted in Figure 2b gives us further confidence in the correctness of the analytical solution presented here.

In addition to the above verifications of simplified scenarios, a numerical model is developed to verify the complete analytical solution (without simplification). The details regarding the implementation of the numerical model are presented in the supporting information (see supporting information). Prior to its use

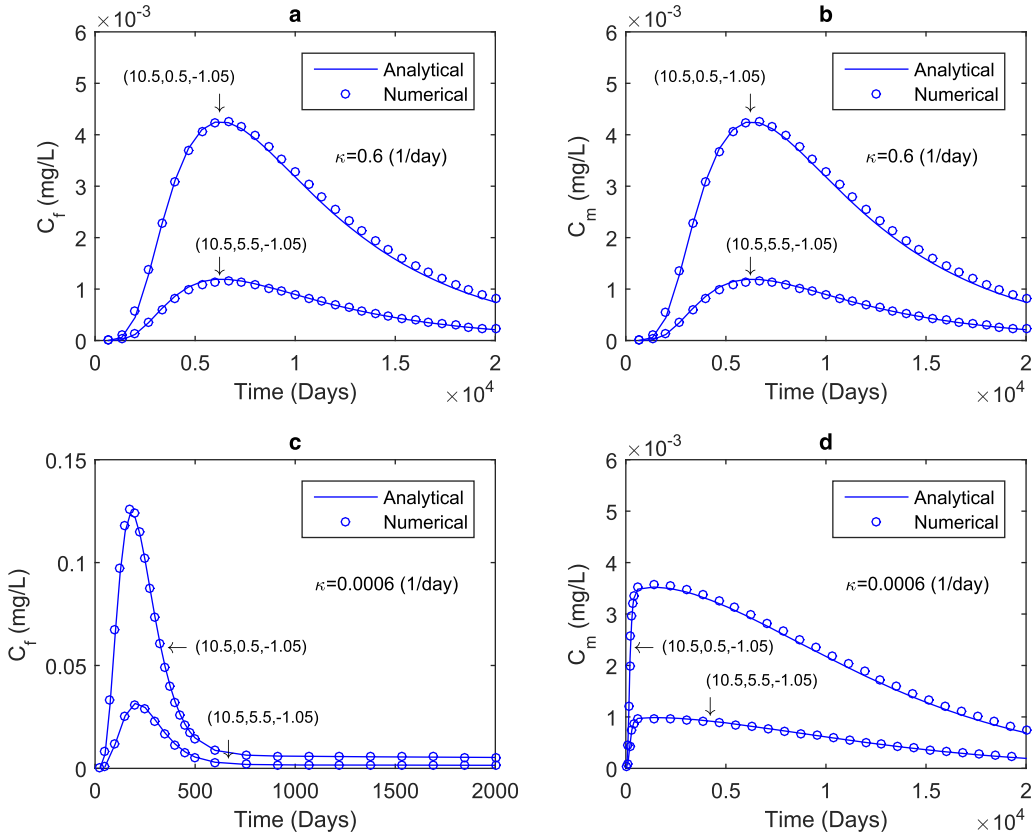

Figure 2c. Concentration breakthrough curves comparing the three-dimensional analytical solution and the numerical model at two down gradient observation points in the fracture system for (a) high and (c) low values of the mass transfer rate coefficient (κ), and comparing the three-dimensional analytical solution and the numerical model at two down gradient observation points in the clay matrix system for (b) high and (d) low values of the mass transfer rate coefficient (κ). The initial concentration distributes in a regular domain (simple initial condition). The numbers in parentheses (*x, y, z*) represent the coordinates (in meters) of the down gradient observation points.

in verifying the unsimplified, complete, analytical solution, the new numerical model is verified by both MT3DMS and the already verified analytical solution for the simplified model scenarios with diffusion in the fractures disabled (see supporting information). The comparison for concentration breakthroughs with two different mass transfer rate coefficients (κ) at two down gradient observation points located in the fracture and clay matrix systems is depicted in Figure 2c. The excellent match with the verified numerical model gives additional confidence in the correctness of the semianalytical solution.

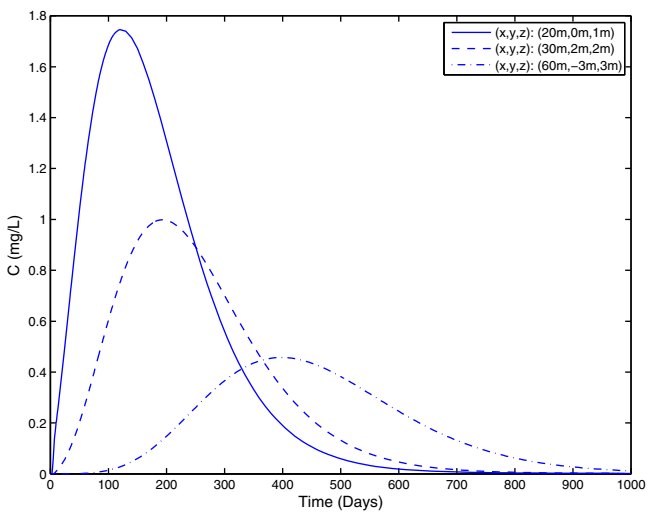

Figure 3. Concentration breakthrough at selected observation locations for the parameters and initial conditions defined in Tables 1 and 2.

4.3. Initial Concentration Distributed Within a Regular Domain

This study characterizes the model solutions for the case in which a DNAPL source does not exist and an initial dissolved concentration is distributed in a specific regular area. The model parameter values used for the simulations are listed in Table 1.

The initial concentration distribution in the aquifer is described by the following functions:

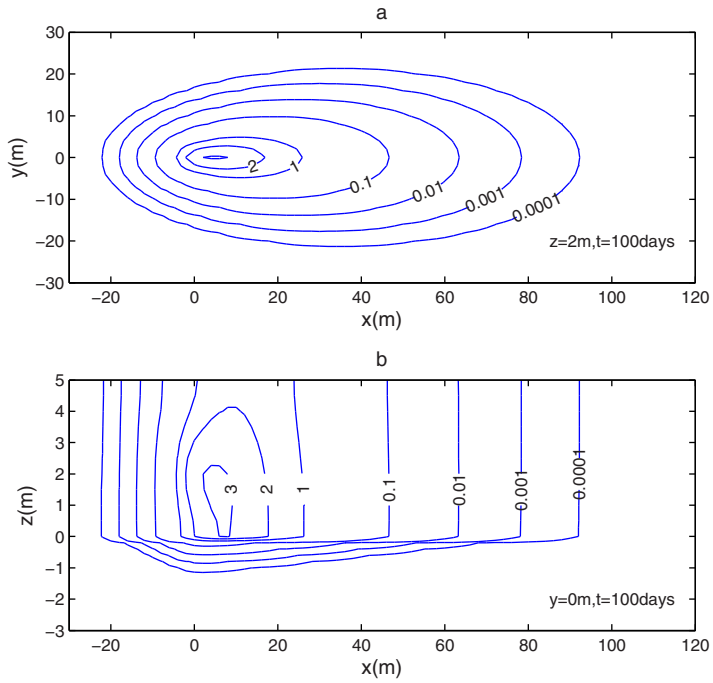

Figure 4. Concentration contours after 100 days of transport at a selected (a) horizontal plane (z = 2 m) and (b) vertical cross section (y = 0 m) for the parameters and initial conditions defined in Tables 1 and 2.

$$f(x,y,z)=\begin{cases} C_0, & x_a \le x \le x_b,\ y_a \le y \le y_b,\ z_a \le z \le z_b \\ 0, & otherwise \end{cases} \tag{26}$$

The geometric parameters used to define the space domain of the initial concentration distribution are listed in Table 2.

Figure 3 shows the concentration breakthrough at several selected observation points for the parameters and initial conditions described above. The concentration displacement was characterized by an initial rapid breakthrough followed by extended tailing at late times due to rate-limited sorption/

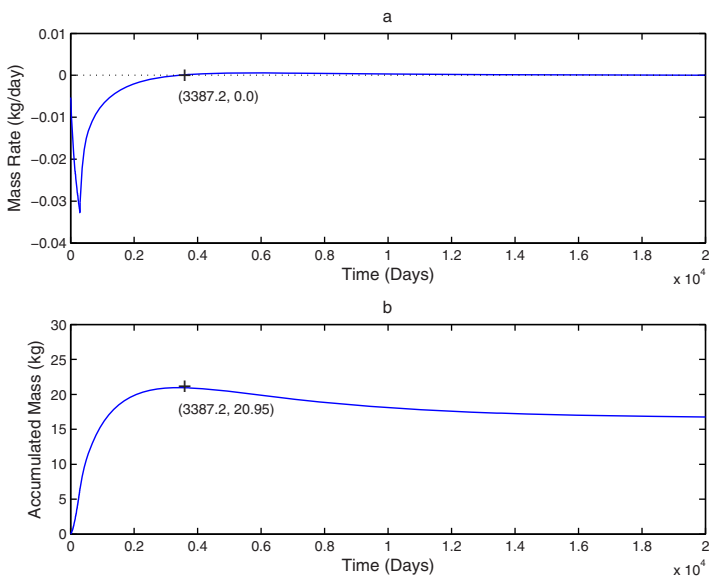

Figure 5. (a) Rate of mass transfer across the bottom plane of the aquifer ($z = 0$) (negative values indicate mass moving from the aquifer into the fractured clay layer) and (b) accumulated mass that passed through the bottom of the aquifer for the parameters and initial conditions defined in Tables 1 and 2.

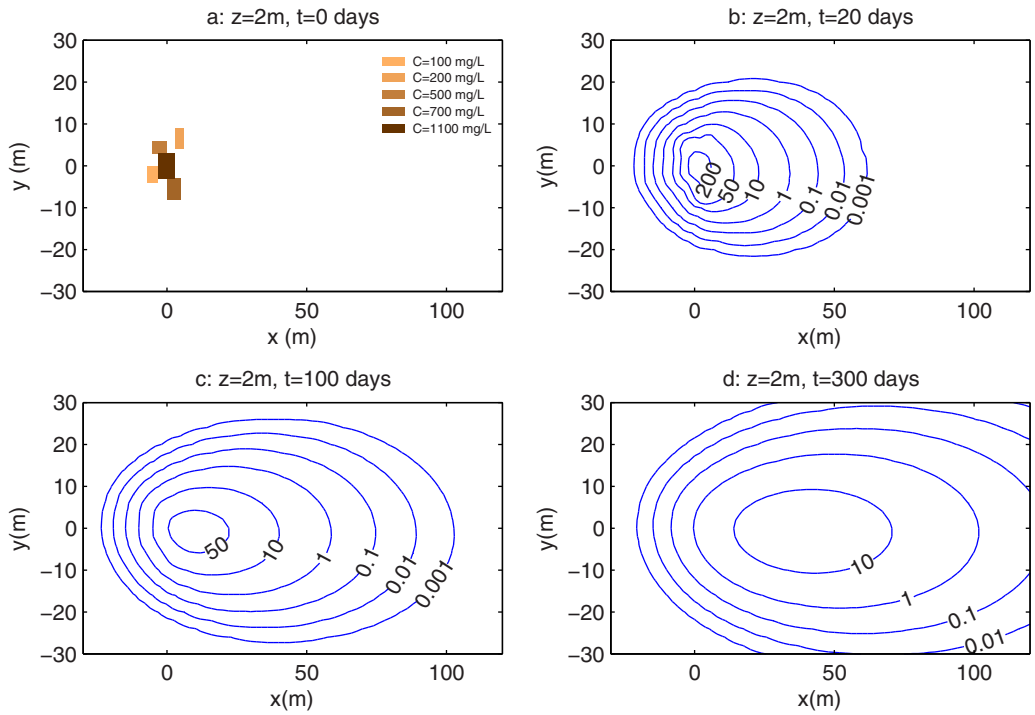

Figure 6. Concentration contours on selected horizontal plane z = 2 m, (a) initial distribution of concentration in rectangles outlined subregions, (b) at day 20, (c) day 100, and (d) day 300 for the case of initial contaminant distribution.

desorption and back diffusion from the fractured clay formation. Figure 4 shows the concentration contours in selected horizontal and vertical planes after 100 days. The concentration plume develops with groundwater flow in the aquifer spanning the top 5 m shown in Figure 4b, while simultaneously migrating into the underlying fractured clay formation ($z < 0$ m) where the concentration contours are deformed reflecting the dual-layer system. Figure 5 shows the rate of mass (r_{mass}) passing through the bottom plane of the aquifer (Figure 5a) and accumulated mass (A_{mass}) that passed through the plane at $z = 0$ (Figure 5b). At early times ($t < 3387$ days), r_{mass} is negative, indicating that mass is moving

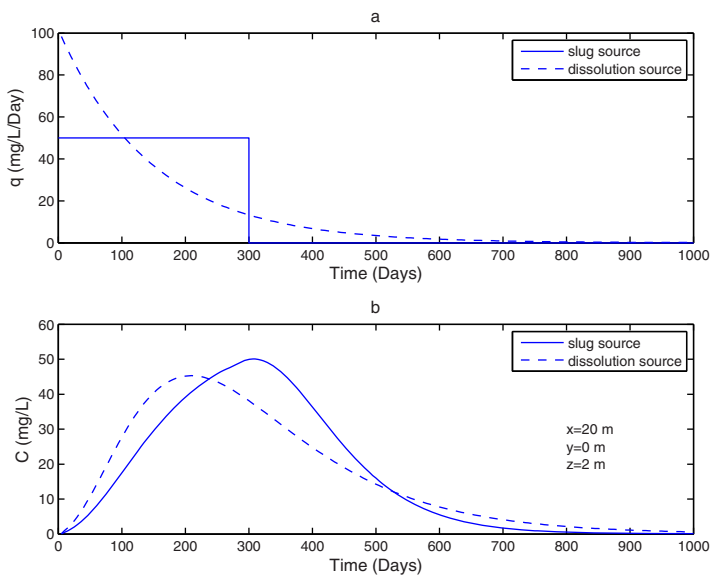

Figure 7. (a) Mass loading rate over time for the slug source and dissolution source, (b) concentration breakthrough at a selected observation location (x = 20 m, y = 0 m, z = 2 m) for the two source functions. Note that mass input for the two sources is equal.

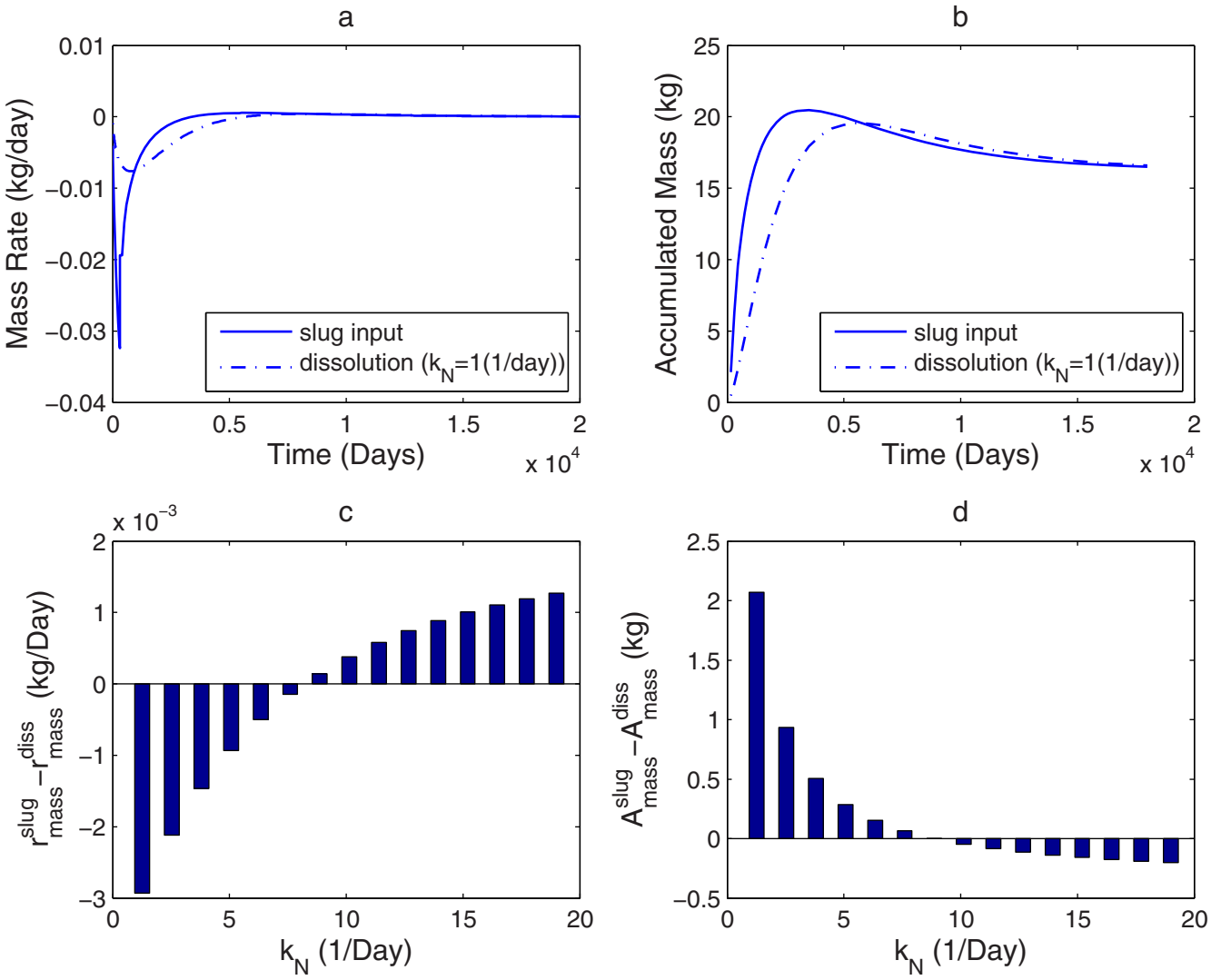

Figure 8. Impact of source type on the mass flux through the bottom plane of the aquifer, (a) rate of mass transfer through the bottom plane of the aquifer (r_{mass}) (negative values indicate mass moving from the aquifer into the fractured clay layer), (b) accumulated mass passed through the bottom plane of the aquifer (A_{mass}), (c) long time-averaged difference of r_{mass} calculated with the two source types versus the dissolution rate coefficient k_N and (d) long time-averaged difference of A_{mass} calculated with the two source types versus k_N.

from the aquifer to the clay, as there is no mass in the clay initially. At later times (t > 3387 days), r_{mass} is slightly positive, indicating that net mass is being slowly released from the clay formation into the aquifer (back diffusion). During the early time period, A_{mass} increases with time, while during back diffusion, A_{mass} decreases with time. Eventually, steady state is attained, when r_{mass} becomes zero, and A_{mass} levels off.

4.4. Nonuniform Initial Concentration Distribution

This section demonstrates the application of the model solution for a more general initial condition. A selected geometric morphology representing the initial distribution of dissolved DNAPL in the aquifer is depicted in Figure 6a, where the rectangles outline the subregions of the source zone in a horizontal plane with thickness 2.0 m (1 m $\leq z \leq$ 3 m), and the color scale on the rectangles indicate the concentration values (mg/L). Figure 6 shows the contours of concentration on the selected horizontal plane at day (b) 20, (c) 100, and (d) 300. At early time (day 20), the irregular initial concentration distribution is reflected by some nonsmooth contours near the source area (Figure 6b) while after some time, dispersion smoothes the concentration contours (Figures 6c and 6d).

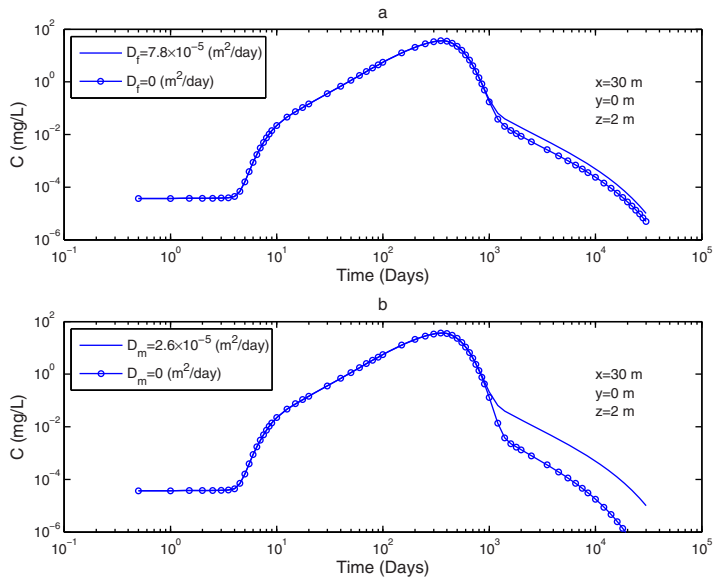

Figure 9. Concentration breakthrough at an observation point for different (a) fracture effective diffusion coefficients (D_f) and (b) matrix effective diffusion coefficients (D_m).

4.5. Time-Dependent Source Function

In this case, it is assumed that there is no initial distribution of contaminant in the aquifer and a time-dependent source exits. The two different types of source functions, a slug mass loading source defined by equation (5) and a dissolving source defined by equation (9), are investigated. The source area switch function g is expressed as:

$$g(x,y,z)=\begin{cases}1, & x_a \le x \le x_b,\ y_a \le y \le y_b,\ z_a \le z \le z_b \\ 0, & \text{otherwise}\end{cases} \tag{27}$$

The source function parameter values used for simulations are listed in Table 3.

Figure 7 shows the mass loading rate (a) and the concentration breakthrough at a specified observation point (b) for two different source functions, slug loading, and dissolution loading. The initial mass input into the aquifer is equal for the two source functions, i.e., $q_0 t_p V_T = \theta \rho_N s_{N0} V_T$. The breakthrough curves reflect the source characteristics. The breakthrough curve for the slug source has a higher peak and exhibits less tailing than the breakthrough curve resulting from the dissolving source. Figure 8 shows the impact of source type on (a) the mass discharge rate through the bottom plane of the aquifer as a function of time (negative values indicate mass discharge downward from the aquifer to the clay), (b) the cumulative mass that passed downward through the plane at the aquifer bottom as a function of time, A_{mass}, (c) the time-averaged difference of r_{mass} calculated with the two source types versus the dissolution rate coefficient k_N, and (d) the time-averaged difference of A_{mass} calculated with the two source types

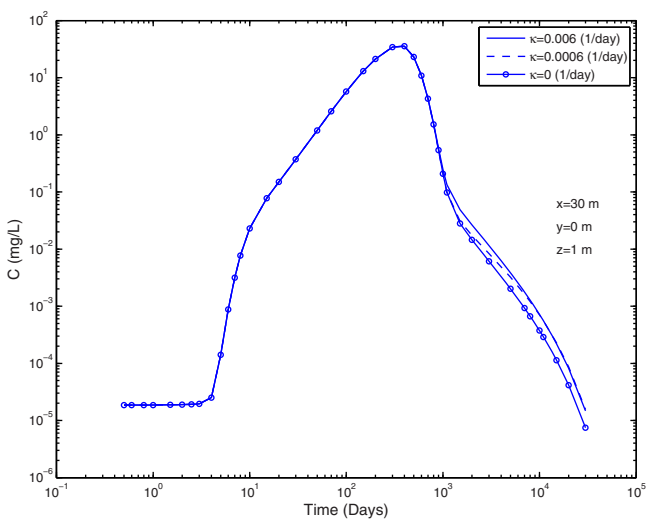

Figure 10. Concentration breakthrough at an observation point for different mass transfer coefficient (κ) of fracture-matrix system.

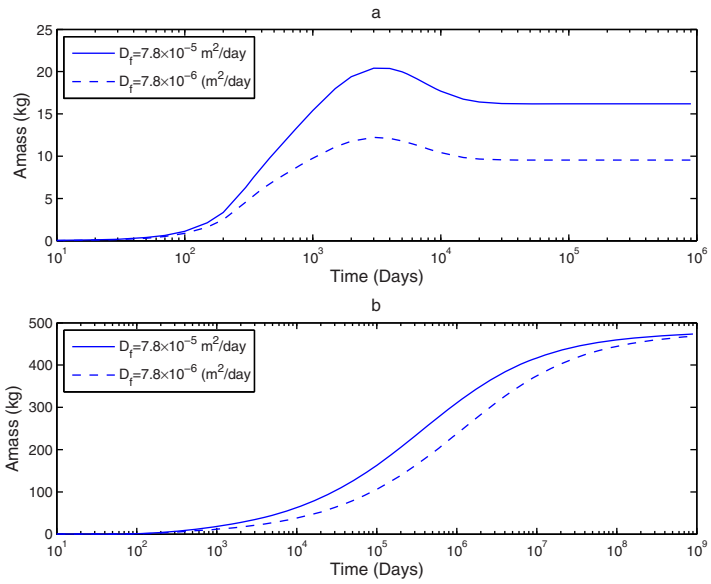

Figure 11. Accumulated mass that passed through the bottom of the aquifer (A_{mass}) for different effective fracture diffusion coefficients (D_f) when: (a) there is degradation in the aquifer (λ_w, λ_s, λ_f, λ_m, and λ_{sm} at their Table 1 values) and (b) there is no degradation in the aquifer (λ_w, λ_s, λ_f, λ_m, and λ_{sm} set to zero).

versus k_N. At early times (before the A_{mass} versus time curve peaks, Figure 8b), r_{mass} is negative (mass moving downward from the aquifer to the clay) and A_{mass} is increasing, which indicates net mass moving into the fractured clay formation. At later times, r_{mass} is slightly positive (back diffusion in an upward direction) and A_{mass} is decreasing. Because the underlying fractured clay is infinite, the contaminant migrates downward (driven by the diffusion process), so A_{mass} remains positive as r_{mass} becomes zero when time approaches infinity (Figure 8b). The time-averaged difference of r_{mass} (Figure 8c) and A_{mass} (Figure 8d) calculated at long times for the two source functions (slug versus dissolving) reveals that at $k_N \approx 9$ day^{-1}, both sources generate the same values of r_{mass} and A_{mass}.

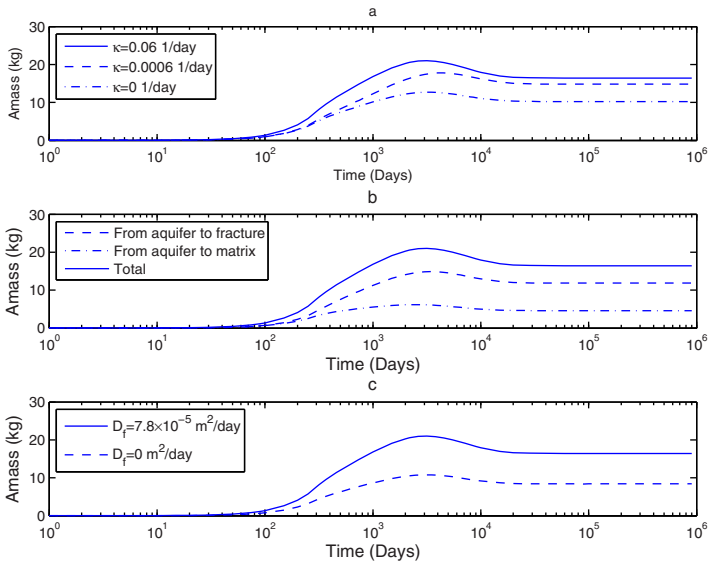

Figure 12. Accumulated mass that passed though the bottom of the aquifer (a) for different fracture-matrix first-order mass transfer coefficients (κ), (b) for κ=0.06 day^{-1}, showing the accumulated mass that passed through fractures versus the mass that entered the matrix directly from the aquifer, and (c) for a matrix with fractures ($D_f = 7.8 \times 10^{-5}$ m^2/d) and κ=0.06 day^{-1} quantifying mass transfer between the fractures and matrix, compared to a matrix without fractures ($D_f = 0$ m^2/d).

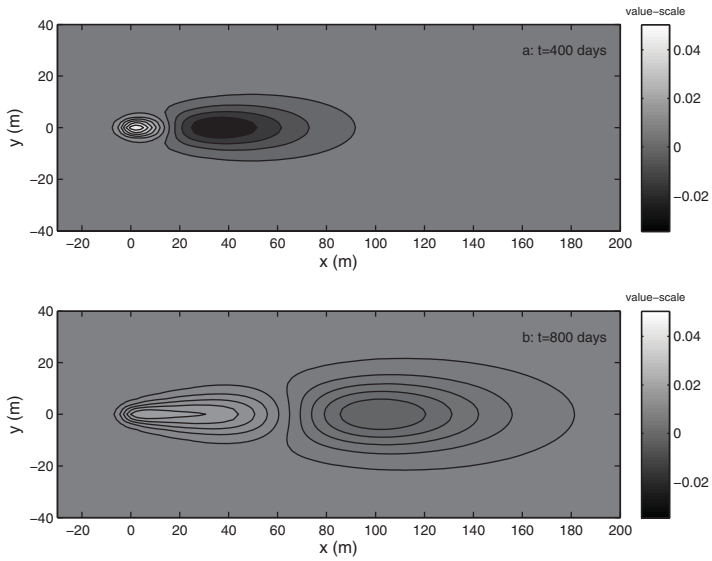

Figure 13. Mass flux across the bottom plane of the aquifer at different times (positive values indicate back-diffusion upward from the fractured clay (g/d/m^2)).

4.6. Effect of Clay Matrix Properties

For the slug mass loading source, the effect of clay matrix properties on the concentration breakthrough is investigated. Figure 9 compares the concentration breakthrough at an observation point for two different fracture effective diffusion coefficients (D_f) and matrix effective diffusion coefficients (D_m). The effect of D_f and D_m becomes obvious at late times (t > 1000 days) with the system having the higher diffusion coefficient exhibiting more "tailing" (higher concentrations at late times). This increased tailing is the result of increased "back diffusion" out of the clay formation due to the higher value of D_f and D_m.

Figure 10 compares the concentration breakthrough at an observation point in the aquifer for three different rate coefficients of mass transfer between the fractures and the matrix (κ). While all the κ values predict similar concentration breakthrough behavior at early times (t < 1000 days), the larger κ value predicts more late time tailing due to more mass being transferred into the clay matrix, resulting in more back diffusion.

Figure 11 compares the effect of the fracture effective diffusion coefficient (D_f) on A_{mass} when there is degradation in the aquifer system (λ_w, λ_s, λ_f, λ_m and λ_{sm} have their Table 1 values) and when there is no degradation (λ_w, λ_s, λ_f, λ_m, and λ_{sm} set to zero). We see from Figure 11a that when there is degradation, at all times there is more mass in the fractured clay at the higher D_f. This makes sense, as the higher value of D_f allows more mass to move out of the aquifer, where degradation is occurring. In the case where there is no degradation in the aquifer, we see from Figure 11b that the long-time value of A_{mass} is independent of the fracture effective diffusion coefficient, and is equal to the mass released into the aquifer ($q_0 t_p V_{source} = 480$ kg for the Tables 2 and 3 parameter values). We also see from Figure 11b that at early times, when there is no decay in the aquifer, A_{mass} is larger for larger values of D_f, as would be expected.

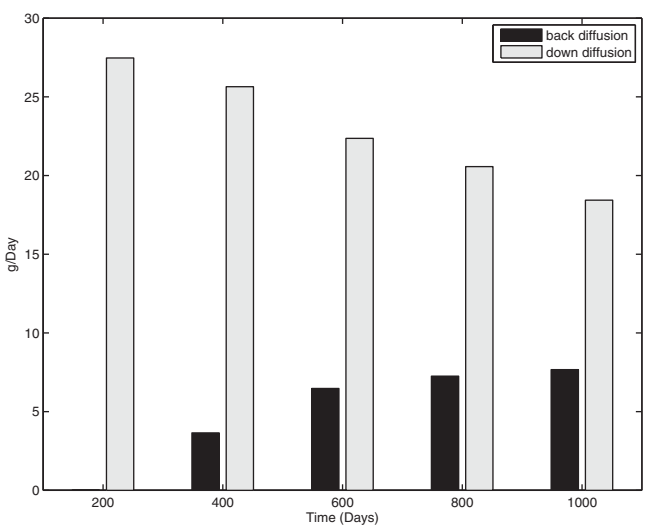

Figure 14. Total rate of mass transfer (g/d) through the bottom plane of the aquifer at different times.

Figure 12a compares the effect of the rate of mass transfer between the fracture and the matrix (κ) on A_{mass}. We see there are considerable differences in the value of A_{mass} at different values of κ. As expected, larger κ values predict larger values of A_{mass} since as more mass is transferred into the matrix as κ increases. Figure 12b differentiates, for κ=0.06 day^{-1}, whether the mass that passed through the aquifer bottom (z = 0) subsequently passed through a fracture, or entered

the matrix directly from the aquifer. We observe the majority of mass passed through the fractures. Figure 12c depicts the difference in A_{mass} over time for systems with and without fractures. Looking at Figures 12b and 12c, it becomes apparent that fracturing has a substantial impact on how much mass resides in the low-permeability zone. In essence, the fractures serve as a shortcut which allows more mass to access the matrix. Without fractures, mass moves into the matrix only by diffusion, which is slowed due to sorption of the contaminant onto matrix solids, as well as the tortuosity of the matrix solids. In contrast, if fractures are present, mass diffuses unhindered through the fractures, and then diffuses into the matrix. Thus, even though the volume of fractures is much smaller than the volume of matrix in the low-permeability zone, the impact of the fractures is large. Clearly, the value of κ, the first-order coefficient quantifying the rate of mass transfer between the fracture and matrix, is important in determining the effect of the fractures. The value of κ used in the Figure 12 simulations is 0.06 day^{-1}. This value is relatively low in comparison to values which have been experimentally estimated. *Polak et al*. [2003] used a model to analyze CT scans of a sodium iodide tracer diffusing from a fracture into a chalk matrix and estimated values for κ that ranged from 4.8 to 7.0 day^{-1}. At these larger values of κ, the effect of the fractures on mass transport would be even greater than observed in the simulations shown here.

4.7. Evolution of Back-Diffusion Zones

For the slug mass loading source, equation (10a), by inverting into the real time domain, can be applied to determine the mass flux ($-D_z\partial C(x,y,z,t)/\partial z$) across the bottom plane of the aquifer (z = 0). Figure 13 shows mass flux contours across the bottom plane of the aquifer at two selected times, where positive values represent back diffusion (upward) and negative values represent downward diffusion from the aquifer into the fractured clay. From the figure, we see how the back-diffusion zones follow the downward-diffusion zones as the plume migrates down gradient. We also observe that back diffusion from the fractured clay in the source zone persists long after the slug mass source is no longer being introduced (recall from Table 3 that the duration of the slug source is 300 days). To assess the overall mass transfer rate out of and into the fractured clay formation, the back-diffusion and downward-diffusion flux are integrated over the area on the plane (z = 0), respectively. Figure 14 shows the overall mass transfer rate in grams per day out of (back diffusion) and into (downward diffusion) the fractured clay as a function of time. At early times (200 days), there is minimal back diffusion, as the slug source ensures a downward concentration gradient. As time goes on, and the source input ends at 300 days, we see back diffusion appears and increases gradually, although over the 1000 day period simulated by the model, downward diffusion dominates. Ultimately, however, back diffusion will dominate.

5. Conclusion

Analytical solutions in the Laplace domain and in real three-dimensional space have been presented for a model that simulates advective, dispersive, and adsorptive transport of a decaying solute in an aquifer underlain by a fractured clay formation. The fractured clay system is conceptualized as a medium characterized by diffusion in the fractures and in the clay matrix, each with a different diffusion coefficient. Mass transfer of the contaminant into the clay formation is demonstrated to be significantly enhanced by the existence of the fractures, even though the volume of fractures is relatively small compared to the volume of the clay matrix. The analytical solutions presented here can be used to analyze contaminant fate and transport in a dual-layer aquifer system with various source zone architectures. The solutions can also be used to assess the mass flux through the aquifer/fractured clay formation interface. Exact analytical solutions such as the ones presented here are valuable tools that can be used to verify numerical codes as well as to enhance understanding of the effect of complex, interacting processes on subsurface transport behavior.

Appendix A: Derivation of Analytical Solutions

Taking the Laplace transform to (2a), (2b), and (2c) with respect to t subject to the initial conditions (3c), (3d), and (3e), we have:

$$D_f\frac{d^2\bar{C}_f}{dz^2}-\mu_f\bar{C}_f-\kappa(\bar{C}_f-\bar{C}_m)=0 \tag{A1}$$

$$D_m \frac{d^2\bar{C}_m}{dz^2} - \theta_m(p+\lambda_m)\bar{C}_m - \rho_m(p+\lambda_{sm})\bar{S}_m + \kappa(\bar{C}_f - \bar{C}_m) = 0 \tag{A2}$$

$$\alpha_m(k_m\bar{C}_m - \bar{S}_m) - (p+\lambda_{sm})\bar{S}_m = 0 \tag{A3}$$

where the variables with the bar indicate the Laplace transform, p is the Laplace transform parameter, and

$$\mu_f(p) = \theta_f(p+\lambda_f) \tag{A4}$$

Substituting (A3) into (A2),

$$D_m \frac{d^2\bar{C}_m}{dz^2} - \mu_m\bar{C}_m + \kappa(\bar{C}_f - \bar{C}_m) = 0 \tag{A5}$$

where,

$$\mu_m(p) = \theta_m(p+\lambda_m) + \rho_m k_m \alpha_m(p+\lambda_{sm})/(p+\lambda_{sm}+\alpha_m) \tag{A6}$$

Note that z is defined in the interval $(0, -\infty)$, substituting z with $z' = -z$ would not alter the form in the equations (A1) and (A5). Using the Fourier Sine transform to (A1) and (A5) with respect to z' subject to the boundary conditions (4c), (4d), and (4e), we have a group of algebra equations:

$$(D_f\varsigma^2 + \mu_f + \kappa)\hat{\bar{C}}_f - \kappa\hat{\bar{C}}_m = D_f\varsigma\bar{C}_{f0} \tag{A7}$$

$$-\kappa\hat{\bar{C}}_f + (D_m\varsigma^2 + \mu_m + \kappa)\hat{\bar{C}}_m = D_m\varsigma\bar{C}_{m0} \tag{A8}$$

where the variables with the hat indicate the Fourier Sine transform, ς is the Fourier Sine transform parameter, $\bar{C}_{f0} = \bar{C}_{m0} = \bar{C}(x, y, 0, p)$.

Directly Solving (A7) and (A8), we have

$$\hat{\bar{C}}_f = \frac{D_f\varsigma(D_m\varsigma^2 + \mu_m + \kappa) + D_m\varsigma\kappa}{(D_f\varsigma^2 + \mu_f + \kappa)(D_m\varsigma^2 + \mu_m + \kappa) - \kappa^2}\bar{C}(x, y, 0, p) \tag{A9}$$

$$\hat{\bar{C}}_m = \frac{D_m\varsigma(D_f\varsigma^2 + \mu_f + \kappa) + D_f\varsigma\kappa}{(D_f\varsigma^2 + \mu_f + \kappa)(D_m\varsigma^2 + \mu_m + \kappa) - \kappa^2}\bar{C}(x, y, 0, p) \tag{A10}$$

Alternatively, (A9) and (A10) can be written as:

$$\hat{\bar{C}}_f = [\frac{F_1\varsigma}{(\varsigma^2 + r_1)} + \frac{F_2\varsigma}{(\varsigma^2 + r_2)}]\bar{C}(x, y, 0, p) \tag{A11}$$

$$\hat{\bar{C}}_m = [\frac{M_1\varsigma}{(\varsigma^2 + r_1)} + \frac{M_2\varsigma}{(\varsigma^2 + r_2)}]\bar{C}(x, y, 0, p) \tag{A12}$$

where

$$F_1 = [D_f(\mu_m + \kappa) + D_m\kappa - D_f D_m r_1]/d \tag{A13}$$

$$F_2 = -[D_f(\mu_m + \kappa) + D_m\kappa - D_f D_m r_2]/d \tag{A14}$$

$$M_1 = [D_m(\mu_f + \kappa) + D_f\kappa - D_f D_m r_1]/d \tag{A15}$$

$$M_2 = -[D_m(\mu_f + \kappa) + D_f\kappa - D_f D_m r_2]/d \tag{A16}$$

$$r_1 = (b-d)/(2D_f D_m) \tag{A17}$$

$$r_2 = (b+d)/(2D_f D_m) \tag{A18}$$

$$b = D_f(\mu_m + \kappa) + D_m(\mu_f + \kappa) \tag{A19}$$

$$d = \{b^2 - 4D_m D_f[\mu_f\mu_m + (\mu_f + \mu_m)\kappa]\}^{1/2} \tag{A20}$$

Note that z' is replaced back to z, the Fourier inverse transforms of (A11) and (A12) are:

$$\bar{C}_f = [F_1 \exp(\sqrt{r_1}z) + F_2 \exp(\sqrt{r_2}z)]\bar{C}(x, y, 0, p) \tag{A21}$$

$$\bar{C}_m=[M_1\exp(\sqrt{r_1}z)+M_2\exp(\sqrt{r_2}z)]\bar{C}(x,y,0,p) \tag{A22}$$

Applying the Laplace transform with respect to t, equations (1a) and (1b) become:

$$D_x\frac{\partial^2\bar{C}}{\partial x^2}-v\frac{\partial\bar{C}}{\partial x}+D_y\frac{\partial^2\bar{C}}{\partial y^2}+D_z\frac{\partial^2\bar{C}}{\partial z^2}-\theta(p+\lambda_w)\bar{C}-\rho_b(p+\lambda_s)\bar{S}=-(\theta+\rho_b k_d)f-\bar{q} \tag{A23}$$

$$\bar{S}=\alpha k_d(p+\lambda_s+\alpha)^{-1}\bar{C}+k_d(p+\lambda_s+\alpha)^{-1}f \tag{A24}$$

Substituting (A24) into (A23),

$$D_x\frac{\partial^2\bar{C}}{\partial x^2}-v\frac{\partial\bar{C}}{\partial x}+D_y\frac{\partial^2\bar{C}}{\partial y^2}+D_z\frac{\partial^2\bar{C}}{\partial z^2}-\mu\bar{C}=-\psi f-\phi g \tag{A25}$$

$$\mu(p)=\theta(p+\lambda_w)+\rho_b k_d\alpha(p+\lambda_s)/(p+\lambda_s+\alpha) \tag{A26}$$

$$\psi(p)=\theta+\rho_b k_d\alpha/(p+\lambda_s+\alpha) \tag{A27}$$

$\phi(p)$ is a function associated with the mass loading rate in the source area. For the slug mass loading,

$$\phi(p)=q_0[1-\exp(-pt_p)]/p \tag{A28}$$

For the dissolution mass loading,

$$\phi(p)=\begin{cases}\theta k_N C_s s_{N0}/(p+\eta), & \sigma=1\\ \theta k_N C_s\int_0^\infty[(\sigma-1)\eta t+s_{N0}^{1-\sigma}]^{\sigma/(1-\sigma)}\exp(-pt)dt, & \sigma\neq 1\end{cases} \tag{A29}$$

In the Laplace domain, the boundary conditions (4a) and (4f) would be

$$\frac{\partial\bar{C}}{\partial z}=0,\ z=B,\ -\infty<x,y<\infty \tag{A30}$$

$$\frac{\partial\bar{C}}{\partial z}-\Delta(p)\bar{C}=0,\ z=0,\ -\infty<x,y<\infty \tag{A31}$$

where

$$\Delta(p)=[D_f(F_1\sqrt{r_1}+F_2\sqrt{r_2})+D_m(M_1\sqrt{r_1}+M_2\sqrt{r_2})]/D_z \tag{A32}$$

Taking the double Fourier transform to (A25) with respect to x and y, we have

$$D_z\frac{\partial^2\tilde{\bar{C}}}{\partial z^2}-[\mu(p)+iv\hat{x}+D_x\hat{x}^2+D_y\hat{y}^2]\tilde{\bar{C}}=H(\hat{x},\hat{y},z,p) \tag{A33}$$

where

$$H(\hat{x},\hat{y},z,p)=-\psi(p)\tilde{f}(\hat{x},\hat{y},z)-\phi(p)\tilde{g}(\hat{x},\hat{y},z) \tag{A34}$$

The variables with tilde represents Fourier transform, $\hat{x}$ and $\hat{y}$ are the Fourier transform parameters.

Nonhomogeneous differential equation (A33) has the general solution:

$$\tilde{\bar{C}}(\hat{x},\hat{y},z,p)=d_1\exp(-rz)+d_2\exp(rz)+u(z) \tag{A35}$$

where d_1 and d_2 are the constants of integration, and $u(z)$ is the particular solution of the nonhomogeneous equation represented as

$$u(z)=-1/(2D_z r)\left\{\int_0^z\exp[r(z'-z)]H(\hat{x},\hat{y},z',p)dz'+\int_z^B\exp[r(z-z')]H(\hat{x},\hat{y},z',p)dz'\right\} \tag{A36}$$

$$r=(D_z)^{-1/2}[\mu(p)+iv\hat{x}+D_x\hat{x}^2+D_y\hat{y}^2]^{1/2} \tag{A37}$$

Applying boundary conditions (A30) and (A31), d_1 and d_2 can be determined,

$$d_1=R[\exp(rB)w_1+w_2]/[\exp(-rB)R+\exp(rB)] \tag{A38}$$

$$d_2=[\exp(-rB)Rw_1-w_2]/[\exp(-rB)R+\exp(rB)] \tag{A39}$$

$$w_1=1/(2D_z r)\int_0^B \exp(-rz')H(\hat{x},\hat{y},z',p)dz' \tag{A40}$$

$$w_2=1/(2D_z r)\int_0^B \exp[r(z'-B)]H(\hat{x},\hat{y},z',p)dz' \tag{A41}$$

$$R=(\Delta-r)/(\Delta+r) \tag{A42}$$

Taking the inverse Fourier transform to (A35), the solution in the Laplace domain can be written as:

$$\bar{C}(x,y,z,p)=\frac{1}{4\pi^2}\int_{-\infty}^{\infty}\int_{-\infty}^{\infty}\tilde{\bar{C}}(\hat{x},\hat{y},z,p)\exp[i(\hat{x}x+\hat{y}y)]d\hat{x}d\hat{y} \tag{A43}$$

Appendix B: Calculation of Function $T(\hat{x},\hat{y},z',x,y)$

Function $T(\hat{x},\hat{y},z',x,y)$ is represented as

$$T(\hat{x},\hat{y},z',x,y)=\int_{-\infty}^{+\infty}\int_{-\infty}^{+\infty}\exp[i\hat{x}(x-x')]\cos[\hat{y}(y-y')]h(x',y',z',p)dx'dy' \tag{B1}$$

Function h contains the initial concentration $f(x,y,z)$ and source function $g(x,y,z)$. Approximated h with a piecewise function which is constant in a space element, we may have,

$$h(z,y,z,p)=\sum_{k=1}^{K}b_k h_k \tag{B2}$$

where K is the total number of space elements, h_k contains the initial concentration value, and source function in the element k, b_k is the basis function defined as:

$$b_k=\begin{cases}1, & x,y,z\in e_k\\ 0, & x,y,z\notin e_k\end{cases}$$

e_k is the space element k. For the interpolation scheme, (B1) can be further written as:

$$\begin{aligned}T(\hat{x},\hat{y},z',x,y)&=\int_{-\infty}^{+\infty}\int_{-\infty}^{+\infty}e^{i\hat{x}(x-x')}\cos[\hat{y}(y-y')]\sum_{k=1}^{K}b_k h_k dx'dy'\\&=\frac{1}{i}\sum_{k=1}^{K}\frac{1}{\hat{x}}\left[e^{i\hat{x}(x-x_{k,2})}-e^{i\hat{x}(x-x_{k,1})}\right]\frac{1}{\hat{y}}\{\sin[\hat{y}(y-y_{k,2})]-\sin[\hat{y}(y-y_{k,1})]\}h_k\end{aligned} \tag{B3}$$

where $x_{k,j}$ and $y_{k,j}$ indicate the coordinates of edge j of element k. Substituting (B3) into (31), the analytical convolution can be implemented, which includes simple integration.

$$\int_{\hat{x}_1}^{\hat{x}_2}\frac{1}{\hat{x}}\left[e^{i\hat{x}(x-x_{k,2})}-e^{i\hat{x}(x-x_{k,1})}\right]d\hat{x}=E_1[-i\hat{x}_1(x-x_{k,2})]-E_1[-i\hat{x}_2(x-x_{k,2})]-\{E_1[-i\hat{x}_1(x-x_{k,1})]-E_1[-i\hat{x}_2(x-x_{k,1})]\} \tag{B4}$$

$$\int_{\hat{y}_1}^{\hat{y}_2}\frac{1}{\hat{y}}\{\sin[\hat{y}(y-y_{k,2})]-\sin[\hat{y}(y-y_{k,1})]\}d\hat{y}=Si[\hat{y}_2(y-y_{k,2})]-Si[\hat{y}_1(y-y_{k,2})]-\{Si[\hat{y}_2(y-y_{k,1})]-Si[\hat{y}_1(y-y_{k,1})]\} \tag{B5}$$

where $E_1(\cdot)$ is the exponential integral function and $Si(\cdot)$ is the sine integral function [*Abramowitz and Stegun*, 1970].

Acknowledgments
MATLAB® codes created for this analysis are available upon request by e-mail: huang.junqi@epa.gov. Portions of this research were sponsored by Strategic Environmental Research and Development Program, project ER-1737. The authors are grateful for the constructive comments from the Editor, two anonymous reviewers, and E. J. M. Veling. The content of this manuscript has not been subject to agency review and does not necessarily represent the view of the sponsoring agency. Additionally, the views expressed in this manuscript are those of the authors and do not reflect the official policy or position of the United States Air Force, Department of Defense, or the U.S. Government.

References

Abramowitz, M., and I. A. Stegun (1970), *Handbook of Mathematical Functions*, Dover, N. Y.
AFCEE (2007), AFCEE Source Zone Initiative Final Report, Brooks City-Base, San Antonio, Tex. [Available at https://clu-in.org/download/contaminantfocus/dnapl/Chemistry_and_Behavior/AFCEE-szi-2007a.pdf, accessed August 13, 2015.]
Arfken, G. (1985), *Mathematical Methods for Physicists*, 3rd ed., Academic, Orlando, Fla.

Ayral, D., M. Oteroa, M. Goltz, and A. Demond (2014), Impact of DNAPL contact on the structure of smectitic clay materials, *Chemosphere*, *95*, 182–187.

Ball, W. P., C. Liu, G. Xia, and D. F. Young (1997), A diffusion-based interpretation of tetrachloroethene and trichloroethene concentration profiles in a groundwater aquitard, *Water Resour. Res.*, *33*(12), 2741–2757.

Bear, J. (1979), *Hydraulics of Groundwater*, McGraw-Hill, N. Y.

Burnell, D. K., B. H. Lester, and J. W. Mercer (2012), Improvements and corrections to AT123D code, *Ground Water*, *50*, 943–953, doi: 10.1111/j.1745-6584.2011.00905.x.

Chang, K. T. (2009), *Computation for Bilinear Interpolation, Introduction to Geographic Information Systems*, 5th ed., McGraw-Hill, N. Y.

Chapman, S. W., and B. L. Parker (2005), Plume persistence due to aquitard back diffusion following dense nonaqueous phase liquid source removal or isolation, *Water Resour. Res.*, *41*, W12411, doi:10.1029/2005WR004224.

Chen, C. S. (1986), Solutions for radionuclide transport from an injection well into a single fracture in a porous formation, *Water Resour. Res.*, *22*(4), 508–518, doi:10.1029/WR022i004p00508.

Clement, T. P., T. R. Gautam, K. K. Lee, M. J. Truex, and G. B. Davis (2004), Modeling of DNAPL-dissolution, rate-limited sorption and biodegradation reactions in groundwater systems, *Bioremediation J.*, *8*(1–2), 47–64, doi:10.1080/10889860490453177.

de Hoog, F. R., J. H. Knight, and A. N. Stokes (1982), An improved method for numerical inversion of Laplace transforms, *SIAM J. Sci. Stat. Comput.*, *3*(3), 357–366.

Falta, R. W., P. S. C. Rao, and N. Basu (2005), Assessing the impacts of partial mass depletion in DNAPL source zones: I. Analytical modeling of source strength functions and plume response, *J. Contam. Hydrol.*, *78*, 259–280.

Feenstra, S., J. A. Cherry, and B. L. Parker (1996), Conceptual Models for the Behavior of Dense Nonaqueous Phase Liquids (DNAPLs) in the Subsurface, *Chapter 2 in Dense Chlorinated Solvents and Other DNAPLs in Groundwater,* edited by J. F. Pankow and J. A. Cherry, Waterloo Press, pp. 53–88.

Goltz, M. N., and P. V. Roberts (1986), Three-dimensional solutions for solute transport in an infinite medium with mobile and immobile zones, *Water Resour. Res.*, *22*(7), 1139–1148.

Goltz, M. N., and P. V. Roberts (1987), Using the method of moments to analyze three-dimensional diffusion-limited solute transport from temporal and spatial perspectives, *Water Resour. Res.*, *23*(8), 1575–1585.

Hollenbeck, K. J. (1998), INVLAP.M: A matlab function for numerical inversion of Laplace transforms by the de Hoog algorithm. [Available at http://www.isva.dtu.dk/staff/karl/invlap.htm.]

Imhoff, P. T., and C. T. Miller (1996), Dissolution fingering during the solubilization of nonaqueous phase liquids in saturated porous media: 1. Model predictions, *Water Resour. Res.*, *32*(7), 1919–1928.

Imhoff, P. T., M. W. Farthing, and C. T. Miller (2003), Modeling NAPL dissolution fingering with upscale mass transfer rate coefficients, *Adv. Water Resour.*, *26*, 1097–1111.

Javandel, J., C. Doughty, and C. F. Tsang (1984), *Groundwater Transport: Handbook of Mathematical Models*, AGU, Washington, D. C.

Liu, C. C., and W. P. W. Ball (2002), Back diffusion of chlorinated solvent contaminants from a natural aquitard to a remediated aquifer under well controlled field conditions: Predictions and measurements, *Ground Water*, *40*, 175−184.

McKay, L. D., J. A. Cherry, and R. W. Gillham (1993), Field experiments in a fractured clay till: 1. Hydraulic conductivity and fracture aperture, *Water Resour. Res.*, *29*(4), 1149–1162.

Oreskes, N., K. Shrader-Frechette, and K. Belitz (1994), Verification, validation, and confirmation of numerical models in the earth sciences, *Science*, *263*, 641–646.

Parker, B. L., S. W. Chapman, and M. A. Guilbeault (2008), Plume persistence caused by back diffusion from thin clay layers in a sand aquifer following TCE source-zone hydraulic isolation, *J. Contam. Hydrol.*, *102*, 86–104.

Parker, J. C., and E. Park (2004), Modeling field-scale dense nonaqueous phase liquid dissolution kinetics in heterogeneous aquifers, *Water Resour. Res.*, *40*, W05109, doi:10.1029/2003WR002807.

Polak, A., A. S. Grader, R. Wallach, and R. Nativ (2003), Chemical diffusion between a fracture and the surrounding matrix: Measurement by computed tomography and modeling, *Water Resour. Res.*, *39*(4), 1106, doi:10.1029/2001WR000813.

Sale, T. C., J. A. Zimbron, and D. S. Dandy (2008), Effects of reduced contaminant loading on downgradient water quality in an idealized two-layer granular porous media, *J. Contam. Hydrol.*, *102*, 72–85.

Seyedabbasi, M. A., C. J. Newell, D. T. Adamson, and T. C. Sale (2012), Relative contribution of DNAPL dissolution and matrix diffusion to the long-term persistence of chlorinated solvent source zones, *J. Contam. Hydrol.*, *134-135*, 69–81.

Wilson, J. L. (1997), Removal of aqueous phase dissolved contamination: Non-chemically enhanced pump-and-treat, in *Subsurface Restoration*, edited by C. H. Ward, J. A. Cherry, and M. R. Scalf, pp. 271–285, CRC Press, Boca Raton, Fla.

Yeh, G. T. (1981), AT123D: Analytical transient one-, two-, and three-dimensional simulation of waste transport in the aquifer system, *Rep. ORNL-5602*, Oak Ridge Natl. Lab., Oak Ridge, Tenn.

Zheng, C., and P. P. Wang (1999), *MT3DMS: A modular threedimensional multi-species transport model for simulation of advection, dispersion and chemical reactions of contaminants in groundwater systems; Documentation and user's guide,* U.S. Army Engineer Research and Development Center Contract Report SERDP-99-1, Vicksburg, Miss.

Zhu, J., and J. F. Sykes (2004), Simple screening models of NAPL dissolution in the subsurface, *J. Contam. Hydrol.*, *72*(1–4), 245–258.